



# Efficient electrocatalytic chlorine evolution under neutral seawater conditions enabled by highly dispersed $\text{Co}_3\text{O}_4$ catalysts on porous carbon

Xina Zhang<sup>a,b,c</sup>, Daxiong Wu<sup>a,\*</sup>, Xiangju Liu<sup>b,c</sup>, Yu Qiu<sup>d</sup>, Zhongli Liu<sup>b,c</sup>, Haijiao Xie<sup>e</sup>, Jizhou Duan<sup>b,c,\*\*</sup>, Baorong Hou<sup>b,c</sup>

<sup>a</sup> College of Materials Science and Engineering, Qingdao University of Science and Technology, Qingdao 266042, China

<sup>b</sup> Key Laboratory of Marine Environmental Corrosion and Bio-fouling, Institute of Oceanology, Chinese Academy of Sciences, Qingdao 266071, China

<sup>c</sup> Open Studio for Marine Corrosion and Protection, Pilot National Laboratory for Marine Science and Technology (Qingdao), Qingdao 266237, China

<sup>d</sup> Shaanxi Key Laboratory of Chemical Reaction Engineering, and College of Chemistry and Chemical Engineering, Yanan University, Yan'an, Shaanxi Province 716000, China

<sup>e</sup> Hangzhou Yanqu Information Technology Co., Ltd, Hangzhou 310003, China

## ARTICLE INFO

### Keywords:

Metal-organic frameworks

$\text{Co}_3\text{O}_4$

Porous structure

CER

Neutral seawater

## ABSTRACT

Chlorine evolution reaction (CER) is fundamental and critical for the conversion of  $\text{Cl}^-$  to  $\text{Cl}_2$  in a seawater environment. However, the selectivity and electrocatalytic activity of non-precious metal-based catalysts in CER remain unsatisfactory. It is still a challenge to develop cost-effective and efficient CER electrocatalysts that can be produced in large scale. Herein, we proposed a metal-organic framework (ZIF-67) as a precursor for the synthesis of  $\text{Co}_3\text{O}_4$  with a high specific surface area (SSA) and porous nano-sized. We then demonstrated for the first time that the porous nano-sized  $\text{Co}_3\text{O}_4$  has high chlorine precipitation activity and stability. The potential (vs. Ag/AgCl) increased slightly from 1.225 to 1.258 V within 24 h of electrocatalytic reaction, and the Faraday efficiencies were higher than 80% at different current densities, indicating significant stability and selectivity. CER mechanism of the  $\text{Co}_3\text{O}_4$  material under neutral seawater conditions was verified to be the Krishtalik mechanism by theoretical calculations.

## 1. Introduction

Electrolytic antifouling occurs by applying a direct current to a specific electrode system to produce an electrochemical reaction that uses the chemicals generated by the reaction to prevent or kill the fouling organism and achieve the purpose of antifouling. Electrolytic anti-fouling technology widely used in industry is the electrolysis of seawater for chlorine production. This means that the chlorine-containing substances (such as  $\text{HClO}$ ,  $\text{ClO}^-$ , and  $\text{Cl}_2$ ) generated by the electrolysis of seawater are used to kill bacteria attached to the surface of vessels and pipelines or to prevent bacteria from adhering to them, thereby achieving antifouling effects [1]. Dimensionally stable anodes (DSAs) are considered the foremost Chlorine evolution reaction (CER) catalysts because they are highly active and stable, showing low corrosion rates and stable operation over several years [2]. The electrodes often used in industrial electrolytic seawater chlorine production

are DSAs based on noble metal oxides, such as  $\text{IrO}_2$  and  $\text{RuO}_2$  [3–6]. Ruthenium, however, tends to form thermodynamically stable species such as soluble ruthenium chlorides, which eventually lead to catalyst deactivation and degradation [7,8].

In general, the disadvantage of limited reserves and high cost limit the larger-scale industrial application of precious metals. Recently, many researchers have made considerable efforts to improve catalyst performance with the premise of reducing or replacing noble metal catalysts [9–14]. For instance, Zhang et al. [15] loaded  $\text{RuO}_2$  on carbon cloth with a larger SSA to compose  $\text{RuO}_2/\text{CC}$ . Lim et al. [16] doped Pt atoms in carbon nanotubes to synthesize Pt/CNTs to reduce the noble metal contents. In addition, Lim et al. [7] introduced  $\text{RuO}_2/\text{Nb:TiO}_2$  nanoparticles by doping to decrease the content of Ru in the catalyst. Other than that, Zhang et al. [17] and Hernandez et al. [2] directly synthesized non-precious metal oxides ( $\text{Co}_3\text{O}_4$  and  $\text{CoSb}_2\text{O}_x$ ) to replace noble metal materials. These studies have all contributed to the

\* Corresponding author.

\*\* Corresponding author at: Key Laboratory of Marine Environmental Corrosion and Bio-fouling, Institute of Oceanology, Chinese Academy of Sciences, Qingdao 266071, China.

E-mail addresses: [dxwu100@163.com](mailto:dxwu100@163.com) (D. Wu), [duanjz@qdio.ac.cn](mailto:duanjz@qdio.ac.cn) (J. Duan).

<https://doi.org/10.1016/j.apcatb.2023.122594>

Received 17 October 2022; Received in revised form 4 January 2023; Accepted 6 March 2023

Available online 9 March 2023

0926-3373/© 2023 Published by Elsevier B.V.

improvement of CER.

Meanwhile, the majority of studies on CER catalysts have been conducted with acidic electrolytes [8,18]. Since the CER process usually occurs with simultaneous process of oxygen evolution reaction (OER), the two are competitive reactions [19,20]:



$$E^\circ_{\text{O}_2/\text{H}_2\text{O}} = 1.229\text{ V vs. RHE}$$



$$E^\circ_{\text{Cl}_2/\text{Cl}^-} = (1.358 + 0.059\text{ pH})\text{ V vs. RHE}$$

It should be noted that equilibrium potential for the OER is pH dependent on the normal hydrogen electrode (NHE) scale and therefore pH-independent of the reversible hydrogen electrode (RHE) scale. The opposite is true for the equilibrium potential of CER, where a decrease in the equilibrium potential is accompanied by an overpotential of 0.059 eV per pH value [21]. Therefore, acidification of the anode electrolyte is usually applied to reduce CER overpotential and inhibit the occurrence of OER. For the anti-fouling system, electrolytic seawater chlorine production is more commonly used in marine applications such as platforms, vessel pipelines, and other open systems with seawater as the medium, making it extremely challenging to achieve electrolyte acidification [22]. A neutral electrolyte requires a catalyst with higher chlorine evolution selectivity compared to acidic conditions, increasing the potential difference between OER and CER. Consequently, CER catalysts are more challenging to be studied under neutral conditions than acidic ones [23,24].

It was found that the activity of catalysts can be further enhanced by proper design and construction of their structure and composition. For this purpose, Metal-Organic Frame (MOFs) materials have been extensively used in catalyst studies due to their excellent spatial structure [25–28]. MOFs materials can act as templates for metal oxides to form polyhedral structures composed of micro-nano particles with mesopores under certain conditions. They have small grain sizes and high SSA. Their properties can be changed by adjusting their grain size and pore size. MOFs have become popular for their porosity and open channels that could provide storage space for electrolytes, increase the contact area of the electrolyte with metal oxides, promote the diffusion of reactants as well as the release of the resulting chlorine, and thus raise catalytic activity [29]. However, the application of MOFs related materials as CER catalysts is rarely reported and the performance of MOFs related materials as CER catalysts remains to be explored.

ZIF-67 is one of the extensively studied materials among the available MOFs due to its high-level active cobalt sites as well as its facile synthesis [30]. Taking advantage of the unique frame structure of ZIF-67, anisotropic porous nano-sized  $\text{Co}_3\text{O}_4$  was prepared by controlling the calcination conditions [31]. As the porous nano-sized  $\text{Co}_3\text{O}_4$  inherits the structural characteristics of ZIF-67, it is also expected to have unique catalytic performance for CER activities, which has not yet been reported in the literature.

Herein, we synthesized ZIF-67 precursors by a simple preparation method and investigated the effects of varying sintering temperatures on the SSA and pore size of the resulting  $\text{Co}_3\text{O}_4$  [32]. For the first time, a series of electrochemical tests were conducted on the prepared porous nano-sized  $\text{Co}_3\text{O}_4$  catalysts in an electrolyte of 0.6 M NaCl to evaluate their catalytic performance for CER activities. Furthermore, for further investigation of the reaction mechanism in neutral NaCl solution, we compared the Gibbs free energy ( $\text{Co}_3\text{O}_4$  (311) crystal plane) based on the Volmer-Heyrovsky, Krishtalik, and Volmer-Tafel mechanisms to derive the optimal reaction mechanism and the corresponding active sites.

## 2. Experimental section

### 2.1. Preparation of electrode

#### 2.1.1. Synthesis of ZIF-67 precursors

The preparation procedure of ZIF-67 can be traced to the synthesis method previously reported in the literature [32]. To begin with, 2.5 mmol of  $\text{Co}(\text{NO}_3)_2 \cdot 6\text{H}_2\text{O}$  (99.9%, Macklin) was added into 50 mL of methanol and stirred until dissolved to obtain a pink solution (solution A). Secondly, 10 mmol of 2-methylimidazole (2-MeIM, 99.9%, Aladdin) was added in 50 mL of methanol and stirred until dissolved to obtain a clear solution (solution B) which was then mixed with solution A and stirred vigorously for 20 min. After stewing for 24 h, the product was collected by centrifugation, washed three times with methanol, and freeze-dried to obtain the ZIF-67 precursors.

#### 2.1.2. Synthesis of porous nano-sized $\text{Co}_3\text{O}_4$

The ZIF-67 precursors were sintered at 300 °C, 350 °C, 400 °C, and 450 °C in nitrogen for 30 min, and then in flowing air for another 30 min. The resulting products ( $\text{Co}_3\text{O}_4$ -X, X stands for sintering temperature) were gathered for further characterization and testing.

#### 2.1.3. Preparation of working electrode

To initiate, 5 mg of porous nano-sized  $\text{Co}_3\text{O}_4$  catalyst was added to 50  $\mu\text{L}$  of isopropanol (99.7%, Sinopharm) and 940  $\mu\text{L}$  of ethanol (99.5%, Sinopharm) and dispersed ultrasonically for 10 min. Then 10  $\mu\text{L}$  of Nafion solution (5 wt%, Aladdin) was added and sonicated to form a suspension. Subsequently, 100  $\mu\text{L}$  suspension was dropped on a hydrophobic carbon cloth ( $0.5 \times 1.0\text{ cm}$ ) and naturally dried. The resulting samples were designated as CC/X, following  $\text{Co}_3\text{O}_4$ -X.

### 2.2. Characterization

The X-ray diffraction (XRD) patterns of  $\text{Co}_3\text{O}_4$ -X were recorded on an XRD diffractometer (PANalytical Xpert-3). The morphology and micro-structure of  $\text{Co}_3\text{O}_4$ -X were studied with scanning electron microscopy (SEM, Hitachi SU-8010) and transmission electron microscopy (TEM, Hitachi JEOL JEM 2100 F). Energy dispersive X-ray spectroscopy (EDS) was employed to record the elemental mappings. Raman spectra were obtained on a Raman spectroscopy (Horiba LabRAM HR Evolution, UK) by using a 10 mW helium-neon laser at 532 nm. X-ray photoelectron spectroscopy (XPS) spectra were recorded on an ESCALAB 250Xi spectrometer. Automatic specific surface and aperture analyzer (ASAP 2020, 200 °C, outgassing time of 8 h) was used to obtain the  $\text{N}_2$  adsorption-desorption isotherm. Ultra-trace analysis of dissolved Co atoms in the solutions was conducted with inductively coupled plasma mass spectrometry (ICP-MS, Agilent 7700, USA).

### 2.3. Electrochemical testing

A CHI 760E electrochemical workstation (Shanghai CH Instrument) was applied to study the CER process. An H-type electrolytic cell separated by a Nafion 117 proton exchange membrane [16] was applied. In the three-electrode system, Ag/AgCl electrode (saturated with KCl) was used as the reference electrode, Pt electrode as the counter electrode, and CC/X as the working electrode. Linear scanning voltammetry (LSV) was operated at  $5\text{ mV}\cdot\text{s}^{-1}$  from 0.8 to 2.0 V (vs. Ag/AgCl) in 0.6 M NaCl solution. Electrochemical active area (ECSA) was estimated by cyclic voltammetry (CV) measurements of the bilayer capacitance ( $C_{dl}$ ) over the range of 1.0–1.1 V (vs. Ag/AgCl) at 20, 40, 60, 80, 100, and 120  $\text{mV}\cdot\text{s}^{-1}$ , respectively. Electrochemical impedance spectroscopy (EIS) measurements were performed at 1.26 V (vs. Ag/AgCl) with a test frequency of  $0.01\text{--}10^6\text{ Hz}$ . The stability of the catalysts was investigated using the chronoamperometry method.

## 2.4. $\text{Cl}_2$ measurement

N, N-diethyl-1,4-phenylenediamine spectrophotometry (DPD colorimetric method) was applied to quantify the amount of active chlorine. Faraday efficiency was calculated using Eq. (3):

$$\text{FE} (\%) = \text{CVnF} \div (\text{M}(\text{Cl}_2)\text{IT}) \quad (3)$$

where C is the concentration of effective chlorine produced ( $\text{g L}^{-1}$ ), V is the volume of electrolyte (L), n is the number of electrons (mol), F is Faraday constant (96485 C), M is the molar mass of chlorine ( $\text{g mol}^{-1}$ ), I is the applied constant current ( $\text{C s}^{-1}$ ), and t is the running time (s).

## 3. Results and discussion

### 3.1. Analysis of structure and morphology

Fig. S1a shows the XRD pattern of ZIF-67, where the peak positions are in agreement with a standard analog peak position. This is consistent with the results of other related reports [33,34]. Fig. 1a presents the XRD patterns of  $\text{Co}_3\text{O}_4\text{-X}$ . The peak positions of  $\text{Co}_3\text{O}_4\text{-X}$  derived from ZIF-67 are in agreement with those of the spinel phase  $\text{Co}_3\text{O}_4$  (PDF#43-1003), indicating the synthesis of spinel phase  $\text{Co}_3\text{O}_4$  with high purity. The correspondent peak positions are  $19.00^\circ$ ,  $31.27^\circ$ ,  $36.84^\circ$ ,  $38.54^\circ$ ,  $44.80^\circ$ ,  $55.65^\circ$ ,  $59.35^\circ$ , and  $65.23^\circ$ , with the related crystalline surface index of (111), (220), (311), (222), (400), (422), (511), and (440), respectively. Notably, as the sintering temperature of ZIF-67 increases, the intensity of the diffractions for  $\text{Co}_3\text{O}_4\text{-X}$  are gradually enhanced, with narrower half-peak width, improved crystallinity, and correspondingly increased grain size. With sintering temperature increases from  $300^\circ$  to  $450^\circ\text{C}$ , grain size gradually increases from 11.1 to 29.5 nm and crystallinity from 45.0% to 65.5%, as presented in Table S1.

The porosity of ZIF-67 and  $\text{Co}_3\text{O}_4\text{-X}$  can be determined from the  $\text{N}_2$  adsorption-desorption isotherm, as presented in Fig. 1b and Fig. S2a-d. Among them, ZIF-67 shows a typical type I isotherm, reflecting the characteristics of microporous adsorbents.  $\text{Co}_3\text{O}_4\text{-X}$  displays typical type IV isotherms with apparent adsorption hysteresis loops, showing that the sintered samples have mesoporous characteristics [35,36]. The SSAs of the samples are 1862.56, 66.80, 58.82, 31.29, and  $18.49 \text{ m}^2 \text{ g}^{-1}$ , and the pore sizes are 1.6, 10.4, 12.6, 7.3, and 17.4 nm, respectively, as listed in Table S2. As it has been pointed out in the literature [37,38], sintering in  $\text{N}_2$  is helpful in maintaining the morphology of ZIF-67 since the resulting carbon may inhibit further contraction of the MOF, and thus facilitates morphology maintenance. Sintering of ZIF-67 leads to the breakage of the binding bonds between organic ligands and Co ions, as well as the decomposition of the organic ligands. The contraction of the framework structure results in a sudden decrease in SSA [30]. As the sintering temperature increases, the grain grows significantly

(Table S1), resulting in further reduction in the SSA. Therefore, the SSA of  $\text{Co}_3\text{O}_4\text{-X}$  is inversely proportional to the sintering temperature. ZIF-67 has very small pore size (1.6 nm). At the sintering temperature of  $300^\circ\text{C}$ , decomposition of the metal-organic framework results in sudden increase in pore size (10.5 nm). The pore size is further enlarged (12.6 nm) at the sintering temperature of  $350^\circ\text{C}$  as the extent of decomposition increases. At the sintering temperature of  $400^\circ\text{C}$ , however, the grain growth is significant (from 11.1 to 23.8 nm, Table S1), leading to reduction in pore size (7.3 nm). The pore size (17.4 nm) increases abnormally at the sintering temperature of  $450^\circ\text{C}$ , due to the inter-diffusion of the generated gases ( $\text{CO}_2$ ,  $\text{H}_2\text{O}$ , and  $\text{N}_2\text{O}_y$ ) inside the organic framework and  $\text{O}_2$  in the environment [39]. As the sintering temperature increases, gas release and inter-diffusion gradually accelerate the formation of cracks and then the internal surface spalling of the framework, leading to larger cavities and a corresponding increase in pore size.

Fig. 2a schematically illustrates the forming mechanism of  $\text{Co}_3\text{O}_4$  from the co-precipitation and subsequently the sintering of the ZIF-67 precursors. The SEM and TEM images of the ZIF-67 precursors are shown in Fig. S1b-c. The ZIF-67 precursors is a rhombic dodecahedron with smooth surface, demonstrating the single crystal feature [39,40]. The grain size is about 100 nm. The HAADF-STEM and the corresponding EDX mappings are shown in Fig. S1d-h, indicating evenly distributed elements of C, Co, and N. The above results verify the successful synthesis of a highly homogeneous ZIF-67 precursor.

The FESEM images of  $\text{Co}_3\text{O}_4\text{-300}$  (Fig. S3a),  $\text{Co}_3\text{O}_4\text{-350}$  (Fig. 2b),  $\text{Co}_3\text{O}_4\text{-400}$  (Fig. S4a) and  $\text{Co}_3\text{O}_4\text{-450}$  (Fig. S5a) show the similar dodecahedral structure which is inherited from ZIF-67. The structure survived the sintering without significant collapse. The surface of  $\text{Co}_3\text{O}_4\text{-X}$  is rougher and the grain size is reduced compared to that of ZIF-67. TEM images of  $\text{Co}_3\text{O}_4\text{-X}$  (Fig. S3b, Fig. 2c, Fig. S4b, and Fig. S5b) show that the sintered sample consists of many small particles connected to each other. There are many pores between the particles formed by the fracture of the metal-organic framework, providing channels for the reaction between the electrolyte and the catalyst [30,39,41]. Grain size distributions (Fig. S3c, Fig. 2d, Fig. S4c, and Fig. S5c) based on TEM observation of  $\text{Co}_3\text{O}_4\text{-X}$  reveal the average grain size increasing from 9.84 nm to 26.01 nm with the increasing sintering temperature (Table S3). Accordingly, the  $\text{N}_2$  adsorption-desorption isotherms (Fig. 1b and Fig. S2) display the gradually decreasing pore size with the increasing sintering temperature. HR-TEM images (Fig. S3d, Fig. 2e, Fig. S4d, and Fig. S5d) of  $\text{Co}_3\text{O}_4\text{-X}$  show the visible lattice stripes corresponding to the (311), (220), and (111) facets of spinel  $\text{Co}_3\text{O}_4$ . Some desirable high index surfaces with low coordination numbers (400) are exposed at  $300^\circ\text{C}$  (Fig. S3d). However, nanocrystals grew at high annealing temperatures and the exposed high-index facets gradually reduced and eventually disappeared. The number of stable facets (311)

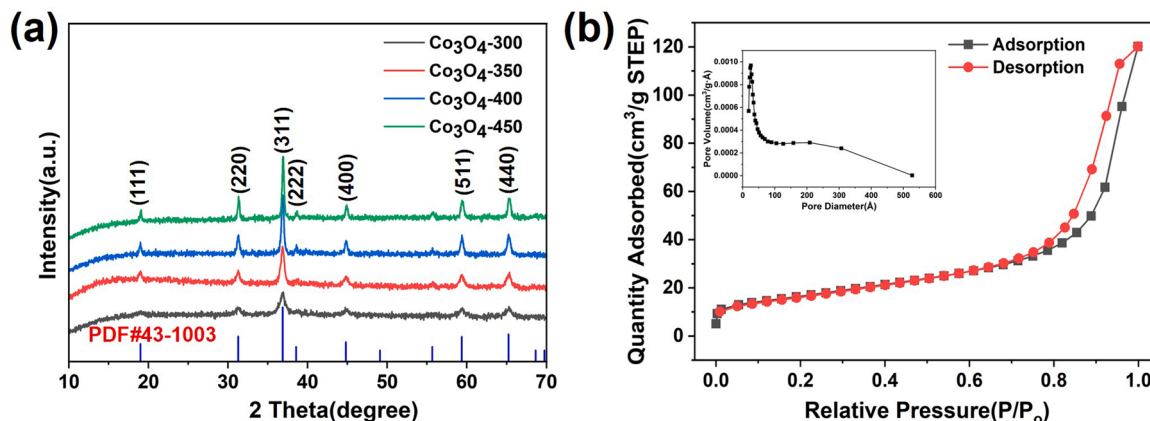


Fig. 1. (a) The XRD patterns of  $\text{Co}_3\text{O}_4\text{-X}$ . (b)  $\text{N}_2$  adsorption-desorption isotherm and pore size distribution plot (inset) of  $\text{Co}_3\text{O}_4\text{-350}$ .



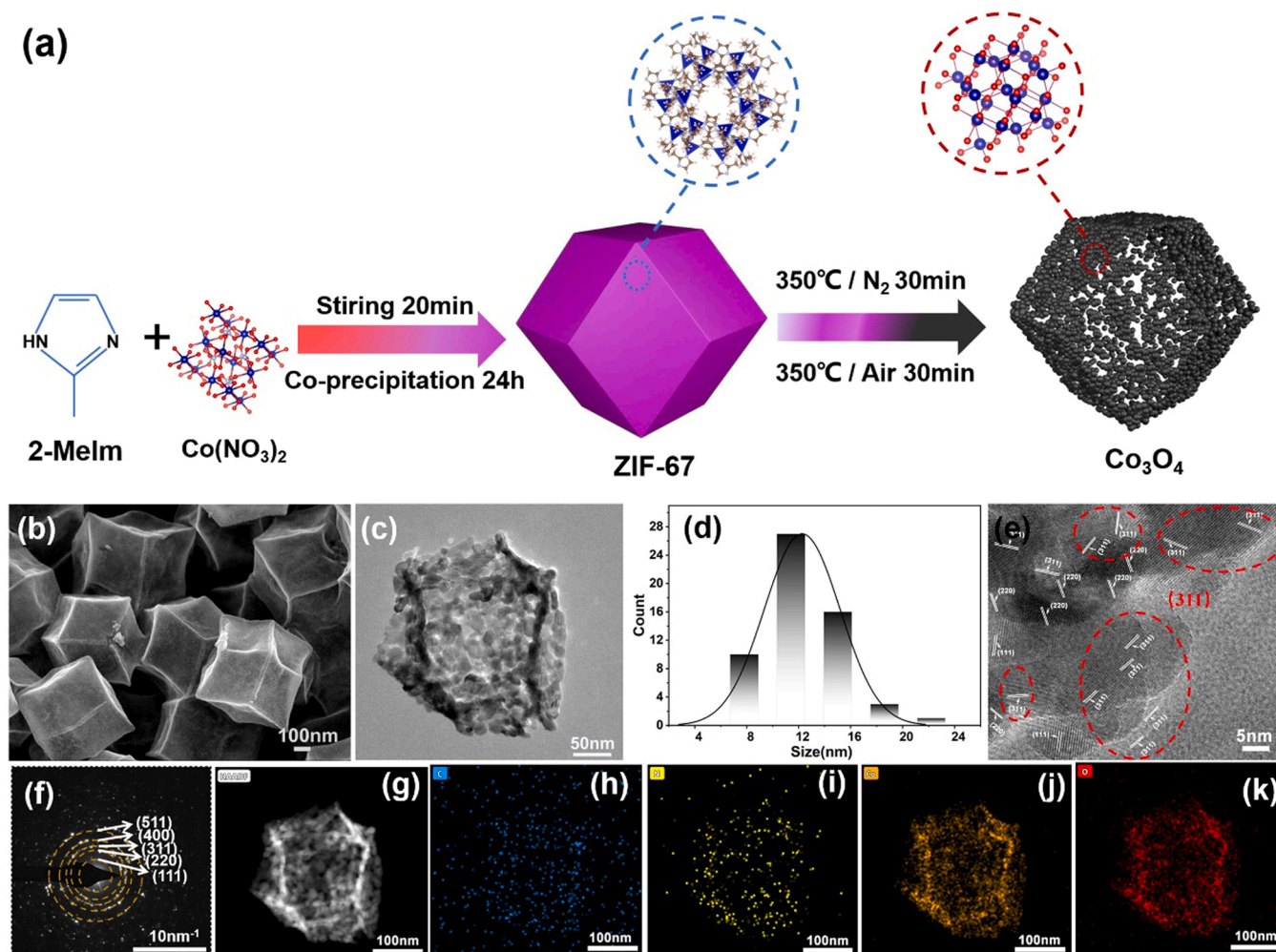


Fig. 2. (a) The schematic illustration of the forming mechanism, (b) FESEM image, (c) TEM image, (d) grain size distribution, (e) HRTEM image, (f) selected area electron diffraction pattern, (g) HAADF-STEM image and EDX mappings of  $\text{Co}_3\text{O}_4$ -350 for (h) C, (i) N, (j) Co, and (k) O.

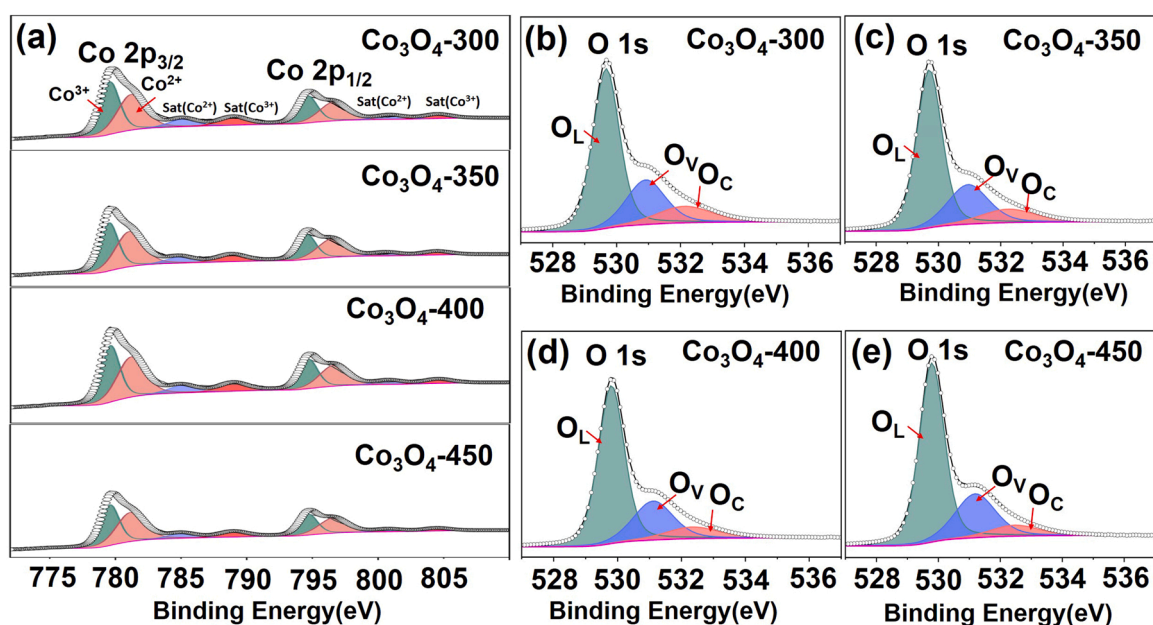


Fig. 3. The XPS spectra of (a) Co 2p and (b-e) O 1s in  $\text{Co}_3\text{O}_4$ -X.

increases accordingly at higher temperatures. That is the main reason for our selection of (311) facets in the DFT theoretical calculations [42]. The selected area electron diffraction pattern (Fig. 2f) of  $\text{Co}_3\text{O}_4$ -350 is in full agreement with the XRD results [41,43]. The HAADF-STEM images and corresponding EDX mappings of  $\text{Co}_3\text{O}_4$ -350 (Fig. 2g-k) and  $\text{Co}_3\text{O}_4$ -300 (Fig. S3e-j) indicate that, with the increase in sintering temperature, trace residues of C, N atoms still exist in the sintered samples. It has been previously reported that ZIF-67 sintered at 350 °C for 3 h cannot achieve complete transformation with carbon residue still exists [44]. Higher sintering temperature and longer sintering time will improve the crystallinity of the sample, resulting in larger grain size, lower SSA, as well as reduced number of active sites that is relevant to the performance of the catalyst.

Research shows that changing the sample sintering temperature not only has a greater effect on the SSA of the sample but also changes the electronic state of the catalyst surface composition, which is another important factor in catalyst research [45]. Fig. 3 and Table S4 present the XPS spectral peaks of Co 2p and O 1s for the  $\text{Co}_3\text{O}_4$ -X. The peaks at 794.58 eV and 779.58 eV can be attributed to the Co 2p<sub>1/2</sub> and Co 2p<sub>3/2</sub>, respectively. The difference in the binding energy (BE) of the two peaks is about 15.4 eV, which is quite consistent with what has been reported in the literature [46–48]. For the Co 2p<sub>3/2</sub> spectrum, the peaks at 780.2 and 781.6 eV are correspondent to the Co<sup>3+</sup> and Co<sup>2+</sup> states, respectively. The spectrum of O 1s is composed of three peaks components: the O<sub>L</sub> component (lattice oxygen) at 530 ± 0.2 eV, the O<sub>V</sub> component (oxygen vacancies) at 531 ± 0.1 eV, and the O<sub>C</sub> component (chemisorbed and dissociated oxygen species of O<sub>2</sub><sup>−</sup>, O<sup>2−</sup>, O<sup>−</sup>) and OH<sup>−</sup>) at 532 ± 0.2 eV. To maintain electrically neutral, the generation of oxygen vacancies is always accompanied by the generation of Co<sup>2+</sup> [49]. Table S4 shows the proportion of O<sub>V</sub>/O<sub>Total</sub> in the O 1s fractional peaks of  $\text{Co}_3\text{O}_4$ -X. We can see that oxygen vacancies and Co<sup>2+</sup> decrease at higher sintering temperatures. Oxygen vacancies decrease due to the further growth and stabilization of microcrystals at higher temperatures. O<sub>V</sub> is beneficial to the adsorption of reactants and is therefore significant for improving electrocatalytic performance. The catalyst activity can be increased by synergizing O<sub>V</sub> with nearby active metal sites in the catalyst. Meanwhile, the active site of CER in  $\text{Co}_3\text{O}_4$  is predicted to be Co<sup>3+</sup> by theoretical calculations in the current work. Fig. S6 shows the calculated Gibbs free energy barriers for Co<sup>2+</sup> and Co<sup>3+</sup> in the rate-determining step (RDS). The Gibbs free energy barrier for Co<sup>3+</sup> (1.86 eV) is significantly lower than that for Co<sup>2+</sup> (2.34 eV). The results evidence that Co<sup>3+</sup> is the active site. The increase in oxygen vacancies leads to a corresponding increase of Co<sup>2+</sup> and results in a decrease in the amount of active sites. In this work, therefore, the influence of SSA is considered to be the main factor contributing to the catalytic

performance, while the chemical state of Co is considered to be a secondary factor. It should also be emphasized that SSA is highly dependent on the sintering temperature, showing a decreasing tendency with increasing sintering temperature, as presented in Table S2.

Fig. 4 shows the Raman spectra of  $\text{Co}_3\text{O}_4$ -X. The standard Raman spectrum of spinel  $\text{Co}_3\text{O}_4$  has an A<sub>1g</sub> band, an E<sub>g</sub> band, and three F<sub>2g</sub> bands, corresponding to peak positions at 684, 477, 616, 519, and 195 cm<sup>−1</sup>, respectively [24]. As shown in Fig. 4, the positions of the peaks of  $\text{Co}_3\text{O}_4$ -X are significantly red-shifted compared to the standard spectrum. Taking the A<sub>1g</sub> vibrational mode as a reference, the wave number reduces from 684 cm<sup>−1</sup> to 677 cm<sup>−1</sup> for  $\text{Co}_3\text{O}_4$ -450, 675 cm<sup>−1</sup> for  $\text{Co}_3\text{O}_4$ -400, 672 cm<sup>−1</sup> for  $\text{Co}_3\text{O}_4$ -350, and 670 cm<sup>−1</sup> for  $\text{Co}_3\text{O}_4$ -300. Such redshift is due to the small grains in the prepared  $\text{Co}_3\text{O}_4$ -X. Lower sintering temperature results in smaller grain size. As previously pointed out in the literature [44,50], redshift in the Raman spectra can be attributed to the optical phonon confinement effect that is closely related to lattice distortion or residual stress in crystallite with small grain size. This is in agree with the conclusion from XPS. The redshift indicates more structural defects in  $\text{Co}_3\text{O}_4$ -X [50].

### 3.2. Electrochemical properties characterization

We evaluated the CER electrocatalytic performance of CC/X in 0.6 M NaCl electrolyte solution using an H-type electrolytic cell. As presented in Fig. 5a, the electrocatalytic activity of CC/X was tested by linear scanning voltammetry (LSV) at a sweep rate of 5 mV/s at the potentials of 0.9–2.0 V (vs. Ag/AgCl). CC/350 has the lowest overpotential and the best electrocatalytic chlorine precipitation activity. Its potential is 1.217 V (vs. Ag/AgCl) at a current density of 10 mA·cm<sup>−2</sup>. The catalytic activity of CER decreases with increasing sintering temperature (from CC/350 to CC/450). As the sintering temperature increases, the SSA reduces, the number of active sites diminishes, and the catalytic activity decreases. However, the catalytic performance of CC/300 is inferior to that of CC/350, mainly due to the lower crystallinity and less active sites in the materials prepared at a sintering temperature of 300 °C. The Tafel slope is commonly applied to study the kinetics of the CER process. Small Tafel slope suggests quick increase in the CER rate and decrease in the overpotential. The lower the value of the Tafel slope, the slower the growth rate of the overpotential. The Tafel slope curves for the CC/X electrode are presented in Fig. 5b. CC/350 has the lowest Tafel slope of 43.31 mV·dec<sup>−1</sup> and CC/300 has the highest Tafel slope of 62.42 mV·dec<sup>−1</sup>. The low value of Tafel slope indicates that CC/350 has excellent CER activity. CC/350 has the fastest electron transfer rate, which facilitates improved interfacial CER kinetics. ECSA is usually proportional to the C<sub>d</sub> of the electrocatalyst. The C<sub>d</sub> is derived from the

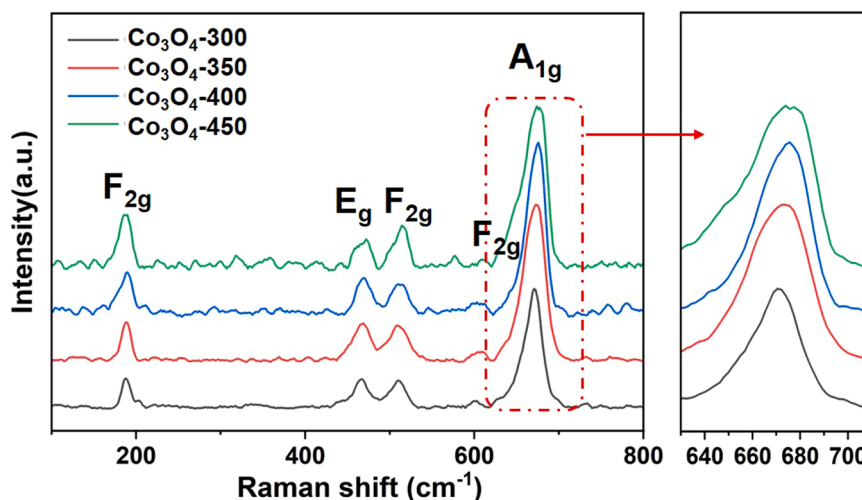
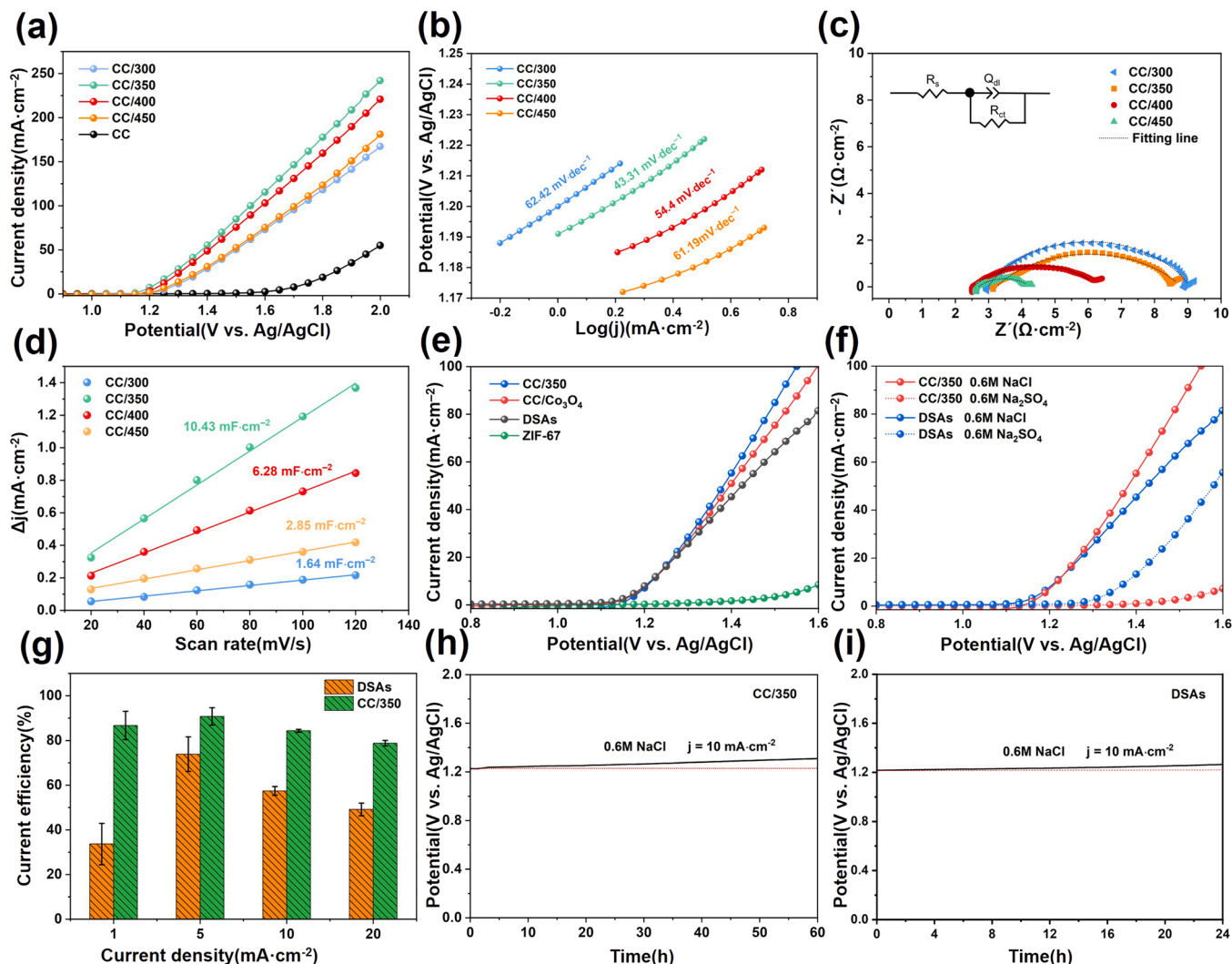


Fig. 4. Raman spectra of  $\text{Co}_3\text{O}_4$ -X and the high-resolution spectra of the A<sub>1g</sub>-activity band.



**Fig. 5.** Electrocatalytic CER performance of the catalysts in 0.6 M NaCl solution. (a) CER polarization curves of CC/X. (b) Tafel slope of CC/X. (c) EIS measurements of CC/X. (d) the capacitive current ( $\Delta j = j_a - j_c$ ) against scan rate for CC/X at 1.05 V. (e) Polarization curves of CC/350, CC/Co<sub>3</sub>O<sub>4</sub>, DSAs, and ZIF-67. (f) Polarization curves of CC/350 and DSAs in 0.6 M NaCl and 0.6 M Na<sub>2</sub>SO<sub>4</sub> electrolyte. (g) The current efficiencies of CC/350 and DSAs at various current densities. (h) Stability test of CC/350. (i) Stability test of DSAs.

CV curve. Electrocatalysts with larger  $C_{dl}$  values show excellent CER activity [51]. In Fig. S7a-d, we derived the  $C_{dl}$  of CC/X by varying the scan rates. With the increase in sintering temperature, the  $C_{dl}$  shows a significant decreasing trend. Among the samples, CC/300 exhibits the smallest  $C_{dl}$  value, indicating the least active sites. The N<sub>2</sub> adsorption-desorption curves show that the specific surface of CC/300 ( $66.8 \text{ m}^2 \cdot \text{g}^{-1}$ ) is two times the SSA of CC/400 ( $31.29 \text{ m}^2 \cdot \text{g}^{-1}$ ). However, its catalytic performance is inferior to that of CC/400. It seems that poor crystallinity of CC/300 reduces the catalytic activity despite its large SSA. In the EIS spectra (Fig. 5c) at 1.26 V (vs. Ag/AgCl), CC/350 shows the smallest capacitive arc radius, suggesting the highest charge transfer efficiency compared to the samples at other sintering temperatures. Taken together, it is concluded that the best electrocatalytic chlorine evolution catalyst can be formed at a sintering temperature of 350 °C.

CER activities of ZIF-67, a commercial DSAs, CC/Co<sub>3</sub>O<sub>4</sub>, and CC/350 were further investigated in a 0.6 M NaCl electrolyte solution and the results are presented in Fig. 5e. Again, CC/350 shows excellent catalytic performance. The CC/Co<sub>3</sub>O<sub>4</sub> catalyst also exhibits good catalytic activity compared to the DSAs, indicating that the non-precious metal catalyst Co<sub>3</sub>O<sub>4</sub> has superior catalytic activity for CER. On the other hand, the grain size of CC/Co<sub>3</sub>O<sub>4</sub> is 50 nm and that of CC/350 is around 200 nm. It seems that the hollow structure of ZIF-67 precursor makes a greater

contribution to the performance of CC/350 as the pores formed during sintering can increase the contact area between catalyst and electrolyte and thus increase the electrocatalytic activity. Given that OER and CER are parallel reactions having the same active sites, [12] the selectivity of the catalyst should be considered as one of the key factors. The catalytic activities of OER and CER of both CC/350 and DSAs were compared in electrolyte solutions of 0.6 M Na<sub>2</sub>SO<sub>4</sub> and 0.6 M NaCl [24]. To achieve satisfactory germicidal efficacy, it is highly desired to have a proper potential difference between CER and OER in order to maintain the required level of active chlorine in seawater. Fig. 5f shows a CER potential of 1.16 V and an OER potential of 1.62 V for CC/350, with the difference of 0.46 V. The CER and OER potentials for the DSAs are 1.22 V and 1.3 V, with a difference of 0.08 V. Thus, it can be seen that CC/350 has better CER selectivity than DSAs (Table S5). Fig. 5g shows the Faraday efficiency for active chlorine generation of the DSAs and CC/350 in a 0.6 M NaCl electrolyte solution at different current densities. The amount of active chlorine generated was quantified by DPD spectrophotometry. The calculation was performed according to Eq. (3), with the applied current densities of 1, 5, 10, and 20 mA·cm<sup>-2</sup>, and the applied current time of 180 s. CC/350 exhibits high selectivity for active chlorine generation in the applied current density range. It is noteworthy that the Faraday efficiencies of both CC/350 and the DSAs



decrease slightly with increasing applied current density, which is unavoidable because of OER competition and current loss at high anode potentials [23]. In spite of this, The Faraday efficiencies of CC/350 are all above 80%, which is better than that of DSA<sub>S</sub>. Suggesting that the selectivity of active chlorine generation in NaCl solution remains at a high level. The electrocatalytic stability of CC/350 was also evaluated and the results are presented in Fig. 5h. The potential of CC/350 increases slightly from 1.225 to 1.258 V at an electrolysis time of 24 h. At 60 h, the potential increases to 1.308 V. As it has been previously pointed out, Co<sub>3</sub>O<sub>4</sub> is thermodynamically stable at the applied potential at which the CER may occur [52]. In the stability test, the dissolved cobalt was quantified by ICP-MS to be 23.4 ug/L, 40.4 ug/L, and 61.9 ug/L at 12 h, 24 h, and 60 h, standing for 0.33%, 0.57%, and 0.86% of the anode catalyst content, respectively.

Fig. 5i shows the stability test of the DSA<sub>S</sub>, where the potential increases from 1.220 to 1.264 V within 24 h. The results indicate that CC/350 has higher selectivity and stability in neutral 0.6 M NaCl electrolyte in comparison to the DSA<sub>S</sub>. We further evaluated the CER activity of CC/350 and the DSA<sub>S</sub> in seawater. As shown in Fig. S8a-b, both CC/350 and the DSA<sub>S</sub> exhibit significant performance in real seawater, while that of CC/350 is superior. The Tafel slopes of CC/350 and the DSA<sub>S</sub> are 88.13 and 102.65 mV·dec<sup>-1</sup>, respectively. CC/350 has a faster electron transfer rate compared to the DSA<sub>S</sub>. The electrocatalytic stability of CC/350 was evaluated by the chronopotentiometry in seawater solution at 5 mA·cm<sup>-2</sup>. As presented in Fig. S8c, the potential increases from 1.215 to 1.264 V (vs. Ag/AgCl) after 70 h of electrolysis, showing high catalytic activity and stability of CC/350 in seawater. For the purpose of electrolytic antifouling, the generated active chlorine can inhibit the growth of bacteria at the level of 0.1 mg/L and kill bacteria at the level of 2 mg/L [22,24,53]. The applied current of 5 mA·cm<sup>-2</sup> was so chosen that the concentration of the generated active chlorine is sufficient to kill bacteria but has minor environmental impact. In the current work, with the applied current of 5 mA·cm<sup>-2</sup> and electrolysis time of 180 s, the concentration of the generated active chlorine in 60 mL of electrolyte solution is 2 mg/L and sufficient to kill surface bacteria and further prevent bacteria from adhering. Therefore, the applied current of 5 mA·cm<sup>-2</sup> is enough for this purpose.

We summarized the catalysts for Chlorine evolution reaction in recent years as shown in Table S6. They are divided into precious metal-based catalysts and non-precious metal-based catalysts. It is easy to find that most of the electrolyte solutions of precious metal-based catalysts are mainly acidic. Lowering the electrolyte solution pH can reduce the Onset potential of CER and thus result in excellent catalytic performance. In recent years, the research on non-precious metal-based catalysts has mainly focused on neutral electrolyte solutions (0.6 M NaCl pH = 6). Compared with the performance of noble metal-based catalysts, it needs to be further improved. The CC/350 studied in this paper has better performance among similar Co<sub>3</sub>O<sub>4</sub> materials, and has little difference in the performance compared to Co<sub>3</sub>O<sub>4</sub> nanoparticles [23]. The potential for CC/350 at 10 mA·cm<sup>-2</sup> is 1.414 V (vs. NHE) compared to 1.40 V (vs. NHE) for Co<sub>3</sub>O<sub>4</sub> nanoparticles. The difference between the two is 14 mV. However, the CC/350 can be operated stably at 10 mA·cm<sup>-2</sup> for 60 h, superior to other similar materials. Therefore, it can be further applied to the electrocatalytic *in-situ* antifouling system for sterilization.

### 3.3. DFT theoretical calculation

As shown in Fig. 6(a), which plots the Gibbs free energy landscapes of the electrocatalytic chlorination reaction on Co<sub>3</sub>O<sub>4</sub> (311) face in different mechanisms in neutral 0.6 M NaCl electrolyte at 1.36 V (vs. RHE), the rate-determining step (RDS) obtained by spin-polarized density functional theory (DFT) calculations are consistent with those reported in previous literature, as described in the Supporting Information.

At 1.36 V (vs. RHE), the Gibbs free energy barriers ( $G_B$ ) are

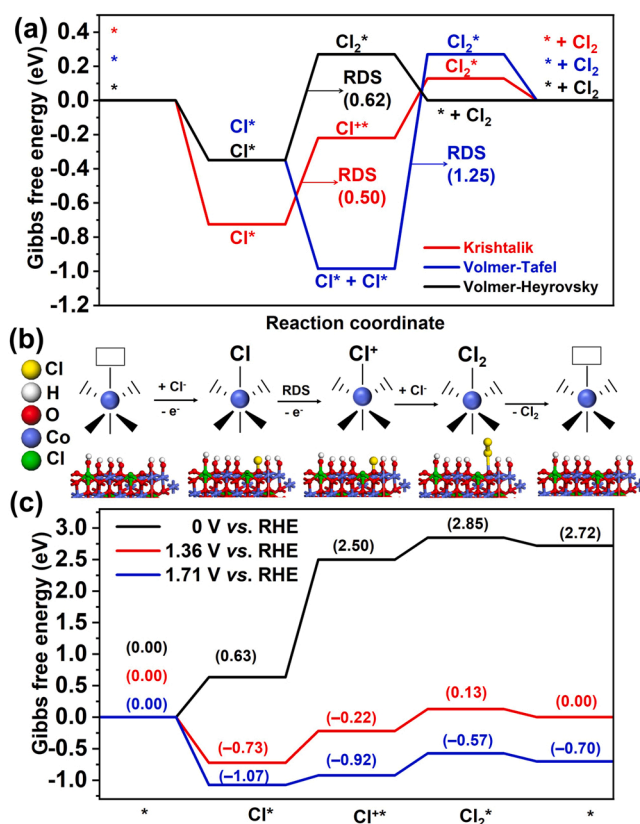


Fig. 6. (a) Gibbs free energy diagram for the chlorine evolution reaction on Co<sub>3</sub>O<sub>4</sub> (311) surface at 1.36 V (vs. RHE) in neutral 0.6 M NaCl electrolyte. The rate-determining step (RDS) and corresponding Gibbs free energy barrier in each mechanism are labeled. (b) Scheme for the electrocatalytic chlorine evolution reaction on Co<sub>3</sub>O<sub>4</sub> (311) surface in Krishtalik mechanism, the optimized geometries for the reaction intermediates are also displayed. (c) Gibbs free energy diagram for the chlorine evolution reaction on Co<sub>3</sub>O<sub>4</sub> (311) surface at 0, 1.36, and 1.71 V (vs. RHE).

calculated to be 0.50 eV for the Krishtalik mechanism, 1.25 eV for the Volmer-Tafel mechanism, and 0.62 eV for the Volmer-Heyrovsky mechanism, respectively. It can be concluded that the Krishtalik mechanism with the lowest Gibbs free energy change ( $\Delta G$ ) for the RDS, is the favorable mechanism for electrocatalytic chlorination reaction. In the meantime, both the reaction sites of Co<sup>2+</sup> and Co<sup>3+</sup> have been considered, and the  $G_B$  is calculated to be 0.98 eV for Co<sup>2+</sup>, and 0.50 eV for Co<sup>3+</sup>. Therefore, the favorable reaction site can be identified to be Co<sup>3+</sup>.

Hence, the reaction mechanism of electrocatalytic chlorine precipitation on the Co<sub>3</sub>O<sub>4</sub> (311) surface in neutral NaCl electrolyte is schematized in Fig. 6(b). The Krishtalik mechanism agree with the results in the previous study [23,54]. The Gibbs free energy diagrams of the chlorine evolution reaction at 0, 1.36, and 1.71 V (vs. RHE) are displayed in Fig. 6(c). The RDS at 0 V (vs. RHE) is also the generation of Cl<sup>+</sup>\*, matching with Fig. 6(a). The  $G_B$  is 1.86 eV at 0 V (vs. RHE). Thus it can be deduced that the onset potential is calculated to be 1.86 V (vs. RHE), matching well with the experimental onset potential of 1.71 V (vs. RHE). At the working potential of 1.71 V (vs. RHE), the  $G_B$  for the chlorine evolution reaction is decreased to 0.35 eV, corresponding to the elementary step of Cl<sup>+</sup>\* + Cl<sup>-</sup> → Cl<sub>2</sub>\*. It should be noted that this elementary step is not an electrochemical reaction that involves electron transfer. The  $G_B$  of 0.35 eV can be well conquered by the kinetic energies of reactants at room temperature. Thus the chlorine evolution reaction can occur at this potential.

In previous literature, some electrocatalysts, like DSAs, RuO<sub>2</sub>(110), prefer the ClO\* pathway, and some other electrocatalysts prefer the Cl\* pathway [55–58]. We also calculated the Krishtalik mechanism

undergoing  $\text{ClO}^*$  pathway for the  $\text{Co}_3\text{O}_4$  (311) face. As is shown in Fig. S10, the rate-determining step is the generation of  $\text{Cl}(\text{O})^*$  with a Gibbs free energy barrier of 2.37 eV at 0 V (vs. RHE), which is higher than that of the  $\text{Cl}^*$  pathway (1.86 eV at 0 V (vs. RHE)). Therefore, It can be concluded that the  $\text{Cl}^*$  pathway, instead of  $\text{ClO}^*$  pathway, is the most favorable for  $\text{Co}_3\text{O}_4$  in the Krishtalik mechanism.

We know that CER and OER are competing reactions. To further illustrate the CER activity of the (311) crystal plane of  $\text{Co}_3\text{O}_4$ , the Oxygen evolution potential of the (311) crystal plane of  $\text{Co}_3\text{O}_4$  was also calculated. The Gibbs free energy diagrams of OER on the  $\text{Co}_3\text{O}_4$  (311) surface is displayed in Fig. S11. The rate-determining step of OER is the generation of  $\text{O}^*$  from  $\text{OH}^*$ , with a Gibbs free energy barrier of 2.10 eV at 0 V (vs. RHE), matching well with the experimental onset potential of 2.17 V (vs. RHE). Therefore, the OER overpotential can be calculated to be 0.87 eV (2.10 eV – 1.23 eV = 0.87 eV). At working potential of 1.71 V (vs. RHE), the Gibbs free energy barrier of OER is calculated to be 0.38 eV, which is still much higher than 0 eV. Therefore, it can be deduced that the OER is not the main reaction under reaction conditions.

#### 4. Conclusions

In summary, ZIF-67 as precursor was synthesized by a simple co-precipitation method and sintered to obtain porous nano-sized  $\text{Co}_3\text{O}_4$ . The obtained CC/350 electrode has high electrocatalytic activity, a low Tafel slope of 43.31  $\text{mV}\cdot\text{dec}^{-1}$ , and excellent stability. In this study, it was found that the porous structure of the sample after sintering provides numerous channels for the contact between electrolyte and catalyst, contributing to rapid charge transfer and collection. The high SSA at low sintering temperatures provides more exposed active sites for catalysis. The catalyst performance is enhanced by the combination of the above factors. It is the first time that the reaction mechanism of  $\text{Co}_3\text{O}_4$  in CER is derived by theoretical calculation, which fills the gap and provides a reference for future investigations.

#### CRedit authorship contribution statement

**Xina Zhang:** Experimental data collection; Data Analysis; Investigation; Writing – original draft. **Daxiong Wu:** Writing – review & editing. **Xiangju Liu:** Data Analysis. **Yu Qiu:** Experimental guidance. **Zhongli Liu:** Experimental methods guidance. **Haijiao Xie:** Theoretical calculation. **Jizhou Duan:** Resources; Financial Support. **Baorong Hou:** Financial Support.

#### Declaration of Competing Interest

The authors declare that they have no known competing financial interests or personal relationships that could have appeared to influence the work reported in this paper.

#### Data Availability

Data available on request.

#### Acknowledgement

This work was supported by the Basic Frontier Science Research Program of Chinese Academy of Sciences (No. ZDBS-LYDQC025).

#### Appendix A. Supporting information

Supplementary data associated with this article can be found in the online version at [doi:10.1016/j.apcatb.2023.122594](https://doi.org/10.1016/j.apcatb.2023.122594).

#### References

- [1] Jitsu Shibata, Mitsuhiro Kimura, Kenji Ueda, Y. Seika, 1972. Ship Hull Anti-Fouling System Utilizing Electrolyzed Sea Water, 80 (1972) 1–9.
- [2] I.A. Moreno-Hernandez, B.S. Brunschwig, N.S. Lewis, Crystalline nickel, cobalt, and manganese antimonates as electrocatalysts for the chlorine evolution reaction, *Energy Environ. Sci.* 12 (2019) 1241–1248, <https://doi.org/10.1039/c8ee03676d>.
- [3] T. Lee, W. Lee, S. Kim, C. Lee, K. Cho, C. Kim, J. Yoon, High chlorine evolution performance of electrochemically reduced  $\text{TiO}_2$  nanotube array coated with a thin  $\text{RuO}_2$  layer by the self-synthetic method, *RSC Adv.* 11 (2021) 12107–12116, <https://doi.org/10.1039/d0ra09623g>.
- [4] J.J. Hu, H.R. Xu, X.D. Feng, L.C. Lei, Y. He, X.W. Zhang, Neodymium-Doped  $\text{IrO}_2$  electrocatalysts supported on titanium plates for enhanced chlorine evolution reaction performance, *ChemElectrochem* 8 (2021) 1204–1210, <https://doi.org/10.1002/celec.202100147>.
- [5] J.H. Huang, M.J. Hou, J.Y. Wang, X. Teng, Y.L. Niu, M.Z. Xu, Z.F. Chen,  $\text{RuO}_2$  nanoparticles decorate belt-like anatase  $\text{TiO}_2$  for highly efficient chlorine evolution, *Electrochim. Acta* 339 (2020), 135878, <https://doi.org/10.1016/j.electacta.2020.135878>.
- [6] M. Chi, B. Luo, Q. Zhang, H. Jiang, C. Chen, S. Wang, D. Min, Lignin-based monolithic carbon electrode decorating with  $\text{RuO}_2$  nanospheres for high-performance chlorine evolution reaction, *Ind. Crops Prod.* 159 (2021), 113088, <https://doi.org/10.1016/j.indcrop.2020.113088>.
- [7] H.W. Lim, D.K. Cho, J.H. Park, S.G. Ji, Y.J. Ahn, J.Y. Kim, C.W. Lee, Rational design of dimensionally stable anodes for active chlorine generation, *ACS Catal.* 11 (2021) 12423–12432, <https://doi.org/10.1021/acscatal.1c03653>.
- [8] H. Dong, W. Yu, M.R. Hoffmann, Mixed metal oxide electrodes and the chlorine evolution reaction, *J. Phys. Chem. C* 125 (2021) 20745–20761, <https://doi.org/10.1021/acs.jpcc.1c05671>.
- [9] W. Tong, M. Forster, F. Dionigi, S. Dressp, R. Sadeghi Erami, P. Strasser, A.J. Cowan, P. Farràs, Electrolysis of low-grade and saline surface water, *Nat. Energy* 5 (2020) 367–377, <https://doi.org/10.1038/s41560-020-0550-8>.
- [10] R.K. Karlsson, A. Cornell, Selectivity between oxygen and chlorine evolution in the chlor-alkali and chlorate processes, *Chem. Rev.* 116 (2016) 2982–3028, <https://doi.org/10.1021/acs.chemrev.5b00389>.
- [11] G. Liu, Y. Xu, T. Yang, L. Jiang, Recent advances in electrocatalysts for seawater splitting, *Nano Mater. Sci.* (2020), <https://doi.org/10.1016/j.nanoms.2020.12.003>.
- [12] Y. Wang, Y. Liu, D. Wiley, S. Zhao, Z. Tang, Recent advances in electrocatalytic chloride oxidation for chlorine gas production, *J. Mater. Chem. A* 9 (2021) 18974–18993, <https://doi.org/10.1039/d1ta02745j>.
- [13] C.E. Finke, S.T. Omelchenko, J.T. Jasper, M.F. Lichterman, C.G. Read, N.S. Lewis, M.R. Hoffmann, Enhancing the activity of oxygen-evolution and chlorine-evolution electrocatalysts by atomic layer deposition of  $\text{TiO}_2$ , *Energy Environ. Sci.* 12 (2019) 358–365, <https://doi.org/10.1039/c8ee02351d>.
- [14] Y. Wang, Y. Xue, C. Zhang, Rational surface and interfacial engineering of  $\text{IrO}_2$  / $\text{TiO}_2$  nanosheet arrays toward high-performance chlorine evolution electrocatalysis and practical environmental remediation, *Small* 17 (2021), e2006587, <https://doi.org/10.1002/sml.202006587>.
- [15] F. Zhang, X. Gu, S. Zheng, H. Yuan, J. Li, X. Wang, Highly catalytic flexible  $\text{RuO}_2$  on carbon fiber cloth network for boosting chlorine evolution reaction, *Electrochim. Acta* 307 (2019) 385–392, <https://doi.org/10.1016/j.electacta.2019.03.187>.
- [16] T. Lim, G.Y. Jung, J.H. Kim, S.O. Park, J. Park, Y.T. Kim, S.J. Kang, H.Y. Jeong, S. K. Kwak, S.H. Joo, Atomically dispersed Pt-N4 sites as efficient and selective electrocatalysts for the chlorine evolution reaction, *Nat. Commun.* 11 (2020) 412, <https://doi.org/10.1038/s41467-019-14272-1>.
- [17] X.L. Zhu, P. Wang, Z.Y. Wang, Y.Y. Liu, Z.K. Zheng, Q.Q. Zhang, X.Y. Zhang, Y. Dai, M.H. Whangbo, B.B. Huang,  $\text{Co}_3\text{O}_4$  nanobelt arrays assembled with ultrathin nanosheets as highly efficient and stable electrocatalysts for the chlorine evolution reaction, *J. Mater. Chem. A* 6 (2018) 12718–12723, <https://doi.org/10.1039/c8ta03689f>.
- [18] P. Adiga, N. Doi, C. Wong, D.M. Santosa, L.-J. Kuo, G.A. Gill, J.A. Silverstein, N. M. Avalos, J.V. Crum, M.H. Engelhard, K.A. Stoerzinger, R.M. Asmussen, The influence of transitional metal dopants on reducing chlorine evolution during the electrolysis of raw seawater, *Appl. Sci.* 11 (2021) 11911, <https://doi.org/10.3390/app112411911>.
- [19] J.G. Vos, Z. Liu, F.D. Speck, N. Perini, W. Fu, S. Cherevko, M.T.M. Koper, Selectivity trends between oxygen evolution and chlorine evolution on iridium-based double perovskites in acidic media, *ACS Catal.* 9 (2019) 8561–8574, <https://doi.org/10.1021/acscatal.9b01159>.
- [20] F. Zhang, L. Yu, L. Wu, D. Luo, Z. Ren, Rational design of oxygen evolution reaction catalysts for seawater electrolysis, *Trends Chem.* 3 (2021) 485–498, <https://doi.org/10.1016/j.trechm.2021.03.003>.
- [21] S. Khatun, H. Hirani, P. Roy, Seawater electrocatalysis: activity and selectivity, *J. Mater. Chem. A* 9 (2021) 74–86, <https://doi.org/10.1039/d0ta08709b>.
- [22] G.W. Hsu, Y.F. Lu, S.Y. Hsu, Effects of electrolysis time and electric potential on chlorine generation of electrolyzed deep ocean water, *J. Food Drug Anal.* 25 (2017) 759–765, <https://doi.org/10.1016/j.jfda.2016.07.001>.
- [23] H. Ha, K. Jin, S. Park, K.G. Lee, K.H. Cho, H. Seo, H.Y. Ahn, Y.H. Lee, K.T. Nam, Highly selective active chlorine generation electrocatalyzed by  $\text{Co}_3\text{O}_4$  nanoparticles: mechanistic investigation through in situ electrokinetic and spectroscopic analyses, *J. Phys. Chem. Lett.* 10 (2019) 1226–1233, <https://doi.org/10.1021/acs.jpclett.9b00547>.
- [24] S. Zhang, J. Xi, J. Wu, P. Wang, F. Lin, D. Zhang, Design of an efficient antifouling strategy for underwater optical window based on chlorine generation, *Colloids*



- Surf. A: Physicochem. Eng. Asp. 634 (2022), 127922, <https://doi.org/10.1016/j.colsurfa.2021.127922>.
- [25] L. Tao, C.-Y. Lin, S. Dou, S. Feng, D. Chen, D. Liu, J. Huo, Z. Xia, S. Wang, Creating coordinatively unsaturated metal sites in metal-organic-frameworks as efficient electrocatalysts for the oxygen evolution reaction: Insights into the active centers, *Nano Energy* 41 (2017) 417–425, <https://doi.org/10.1016/j.nanoen.2017.09.055>.
- [26] M. Abdul Nasir Khan, P. Kwame Klu, C. Wang, W. Zhang, R. Luo, M. Zhang, J. Qi, X. Sun, L. Wang, J. Li, Metal-organic framework-derived hollow  $\text{Co}_3\text{O}_4$ /carbon as efficient catalyst for peroxymonosulfate activation, *Chem. Eng. J.* 363 (2019) 234–246, <https://doi.org/10.1016/j.cej.2019.01.129>.
- [27] P. Dai, Y. Yao, E. Hu, D. Xu, Z. Li, C. Wang, Self-assembled ZIF-67@graphene oxide as a cobalt-based catalyst precursor with enhanced catalytic activity toward methanolysis of sodium borohydride, *Appl. Surf. Sci.* 546 (2021), 149128, <https://doi.org/10.1016/j.apsusc.2021.149128>.
- [28] L. Wang, Z. Du, X. Bai, Y. Lin, Constructing macroporous C/Co composites with tunable interfacial polarization toward ultra-broadband microwave absorption, *J. Colloid Interface Sci.* 591 (2021) 76–84, <https://doi.org/10.1016/j.jcis.2021.01.090>.
- [29] B. Li, K. Igawa, J. Chai, Y. Chen, Y. Wang, D.W. Fam, N.N. Tham, T. An, T. Konno, A. Sng, Z. Liu, H. Zhang, Y. Zong, String of pyrolyzed ZIF-67 particles on carbon fibers for high-performance electrocatalysis, *Energy Storage Mater.* 25 (2020) 137–144, <https://doi.org/10.1016/j.ensm.2019.10.021>.
- [30] H. Wen, S. Zhang, T. Yu, Z. Yi, R. Guo, ZIF-67-based catalysts for oxygen evolution reaction, *Nanoscale* 13 (2021) 12058–12087, <https://doi.org/10.1039/d1nr01669e>.
- [31] L. Zhang, Z. Jin, N. Tsubaki, Zeolitic Imidazolate Framework-67-Derived P-Doped Hollow Porous  $\text{Co}_3\text{O}_4$  as a photocatalyst for hydrogen production from water, *ACS Appl. Mater. Interfaces* 13 (2021) 50996–51007, <https://doi.org/10.1021/acsami.1c14987>.
- [32] X. Cai, F. Peng, X. Luo, X. Ye, J. Zhou, X. Lang, M. Shi, Understanding the evolution of cobalt-based metal-organic frameworks in electrocatalysis for the oxygen evolution reaction, *ChemSusChem* 14 (2021) 3163–3173, <https://doi.org/10.1002/cssc.202100851>.
- [33] J. Zhong, Y. Zeng, M. Zhang, W. Feng, D. Xiao, J. Wu, P. Chen, M. Fu, D. Ye, Toluene oxidation process and proper mechanism over  $\text{Co}_3\text{O}_4$  nanotubes: Investigation through in-situ DRIFTS combined with PTR-TOF-MS and quasi in-situ XPS, *Chem. Eng. J.* 397 (2020), 125375, <https://doi.org/10.1016/j.cej.2020.125375>.
- [34] K. Chen, S. Bai, H. Li, Y. Xue, X. Zhang, M. Liu, J. Jia, The  $\text{Co}_3\text{O}_4$  catalyst derived from ZIF-67 and their catalytic performance of toluene, *Appl. Catal. A: Gen.* 599 (2020), 117614, <https://doi.org/10.1016/j.apcata.2020.117614>.
- [35] Y. Qiu, L. Chai, Y. Su, P. Li, W. Yuan, H. Li, X. Guo, One-dimensional hierarchical  $\text{MoO}_2$ - $\text{MoS}_x$  hybrids as highly active and durable catalysts in the hydrogen evolution reaction, *Dalton Trans.* 47 (2018) 6041–6048, <https://doi.org/10.1039/c8dt00779a>.
- [36] J. Su, G. Xia, R. Li, Y. Yang, J. Chen, R. Shi, P. Jiang, Q. Chen,  $\text{Co}_3\text{ZnCo}$ /Co nano heterojunctions encapsulated in N-doped graphene layers derived from PBAs as highly efficient bi-functional OER and ORR electrocatalysts, *J. Mater. Chem. A* 4 (2016) 9204–9212, <https://doi.org/10.1039/c6ta00945j>.
- [37] T. Shu, H. Wang, Q. Li, Z. Feng, F. Wei, K.X. Yao, Z. Sun, J. Qi, Y. Sui, Highly stable  $\text{Co}_3\text{O}_4$  nanoparticles/carbon nanosheets array derived from flake-like ZIF-67 as an advanced electrode for supercapacitor, *Chem. Eng. J.* 419 (2021), 129631, <https://doi.org/10.1016/j.cej.2021.129631>.
- [38] X. Xu, R. Cao, S. Jeong, J. Cho, Spindle-like mesoporous  $\alpha\text{-Fe}_2\text{O}_3$  anode material prepared from MOF template for high-rate lithium batteries, *Nano Lett.* 12 (2012) 4988–4991, <https://doi.org/10.1021/nl302618s>.
- [39] R. Wu, X. Qian, X. Rui, H. Liu, B. Yadian, K. Zhou, J. Wei, Q. Yan, X.Q. Feng, Y. Long, L. Wang, Y. Huang, Zeolitic imidazolate framework 67-derived high symmetric porous  $\text{Co}_3\text{O}_4$  hollow dodecahedra with highly enhanced lithium storage capability, *Small* 10 (2014) 1932–1938, <https://doi.org/10.1002/sml.201303520>.
- [40] Y. Bao, W.-D. Oh, T.-T. Lim, R. Wang, R.D. Webster, X. Hu, Surface-nucleated heterogeneous growth of zeolitic imidazolate framework – A unique precursor towards catalytic ceramic membranes: Synthesis, characterization and organics degradation, *Chem. Eng. J.* 353 (2018) 69–79, <https://doi.org/10.1016/j.cej.2018.07.117>.
- [41] K. Zhao, H. Li, S. Tian, W. Yang, X. Wang, A. Pang, C. Xie, D. Zeng, A facile low-temperature synthesis of hierarchical porous  $\text{Co}_3\text{O}_4$  micro/nano structures derived from ZIF-67 assisted by ammonium perchlorate, *Inorg. Chem. Front.* 6 (2019) 715–722, <https://doi.org/10.1039/c8qi01279b>.
- [42] J. Su, R. Ge, K. Jiang, Y. Dong, F. Hao, Z. Tian, G. Chen, L. Chen, Assembling ultrasmall copper-doped ruthenium oxide nanocrystals into hollow porous polyhedra: highly robust electrocatalysts for oxygen evolution in acidic media, *Adv. Mater.* (2018), e1801351, <https://doi.org/10.1002/adma.201801351>.
- [43] Y. Fu, X. Guo, Z. Xu, G. Zhao, C. Xu, Y. Zhu, L. Zhou, Nanostructure-Mediated phase evolution in lithiation/Delithiation of  $\text{Co}_3\text{O}_4$ , *ACS Appl. Mater. Interfaces* 13 (2021) 28171–28180, <https://doi.org/10.1021/acsami.1c05591>.
- [44] Y. Lu, W. Zhan, Y. He, Y. Wang, X. Kong, Q. Kuang, Z. Xie, L. Zheng, MOF-templated synthesis of porous  $\text{Co}_3\text{O}_4$  concave nanocubes with high specific surface area and their gas sensing properties, *ACS Appl. Mater. Interfaces* 6 (2014) 4186–4195, <https://doi.org/10.1021/am405858v>.
- [45] T. Wu, M.Y. Han, Z.J. Xu, Size effects of electrocatalysts: more than a variation of surface area, *ACS Nano* (2022) 8531–8539, <https://doi.org/10.1021/acsnano.2c04603>.
- [46] J. González-Prior, R. López-Fonseca, J.I. Gutiérrez-Ortiz, B. de Rivas, Oxidation of 1,2-dichloroethane over nanocube-shaped  $\text{Co}_3\text{O}_4$  catalysts, *Appl. Catal. B: Environ.* 199 (2016) 384–393, <https://doi.org/10.1016/j.apcatb.2016.06.046>.
- [47] S.A. Singh, G. Madras, Detailed mechanism and kinetic study of CO oxidation on cobalt oxide surfaces, *Appl. Catal. A: Gen.* 504 (2015) 463–475, <https://doi.org/10.1016/j.apcata.2014.10.024>.
- [48] S. Mo, S. Li, J. Li, Y. Deng, S. Peng, J. Chen, Y. Chen, Rich surface Co(III) ion-enhanced Co nanocatalyst benzene/toluene oxidation performance derived from Co(II)Co(III) layered double hydroxide, *Nanoscale* 8 (2016) 15763–15773, <https://doi.org/10.1039/c6nr04902h>.
- [49] H. Chen, M. Yang, S. Tao, G. Chen, Oxygen vacancy enhanced catalytic activity of reduced  $\text{Co}_3\text{O}_4$  towards p-nitrophenol reduction, *Appl. Catal. B: Environ.* 209 (2017) 648–656, <https://doi.org/10.1016/j.apcatb.2017.03.038>.
- [50] S. Mo, Q. Zhang, S. Li, Q. Ren, M. Zhang, Y. Xue, R. Peng, H. Xiao, Y. Chen, D. Ye, Integrated cobalt oxide based nanoarray catalysts with hierarchical architectures: in situ Raman spectroscopy investigation on the carbon monoxide reaction mechanism, *ChemCatChem* 10 (2018) 3012–3026, <https://doi.org/10.1002/cctc.201800363>.
- [51] Y. Qiu, S. Liu, C. Wei, J. Fan, H. Yao, L. Dai, G. Wang, H. Li, B. Su, X. Guo, Synergistic effect between platinum single atoms and oxygen vacancy in  $\text{MoO}_2$  boosting pH-Universal hydrogen evolution reaction at large current density, *Chem. Eng. J.* 427 (2022), <https://doi.org/10.1016/j.cej.2021.131309>.
- [52] A.R. Zeradjanin, N. Menzel, P. Strasser, W. Schuhmann, Role of water in the chlorine evolution reaction at  $\text{RuO}_2$ -based electrodes—understanding electrocatalysis as a resonance phenomenon, *ChemSusChem* 5 (2012) 1897–1904, <https://doi.org/10.1002/cssc.201200193>.
- [53] R. Pang, Y. Misaki, S. Okunaka, K. Sayama, Photocatalytic production of hypochlorous acid over Pt/ $\text{WO}_3$  under simulated solar light, *ACS Sustain. Chem. Eng.* 8 (2020) 8629–8637, <https://doi.org/10.1021/acssuschemeng.0c01341>.
- [54] R. Boggio, A. Carugati, G. Lodi, S. Trasatti, Mechanism & study of  $\text{Cl}_2$  evolution at Ti-supported  $\text{Co}_3\text{O}_4$  anodes, *J. Appl. Electrochem.* (1983) 335–349, <https://doi.org/10.1007/BF00615986>.
- [55] J.J.H. Junxian Liu, Huajie Yin, Porun Liu, Huijun Zhao, Yun Wang,  $\beta$ -Arsenene Monolayer: a promising electrocatalyst for anodic chlorine evolution reaction, *Catalysts* (2022), <https://doi.org/10.3390/catal12030296>.
- [56] K.S. Exner, J. Anton, T. Jacob, H. Over, Chlorine evolution reaction on  $\text{RuO}_2(110)$ : Ab initio atomistic thermodynamics study - Pourbaix diagrams, *Electrochim. Acta* 120 (2014) 460–466, <https://doi.org/10.1016/j.electacta.2013.11.027>.
- [57] J. Liu, J.J. Hirsch, H. Yin, P. Liu, H. Zhao, Y. Wang, TMN4 complex embedded graphene as efficient and selective electrocatalysts for chlorine evolution reactions, *J. Electroanal. Chem.* 907 (2022), <https://doi.org/10.1016/j.jelechem.2022.116071>.
- [58] J. Liu, J.J. Hirsch, H. Yin, P. Liu, H. Zhao, Y. Wang, Low-Dimensional metal-organic frameworks with high activity and selectivity toward electrocatalytic chlorine evolution reactions, *J. Phys. Chem. C* 126 (2022) 7066–7075, <https://doi.org/10.1021/acs.jpcc.2c01593>.